

# Ultrafast laser-driven quantum dynamics in positronium chloride

Einar Aurbakken,<sup>1</sup> Håkon Emil Kristiansen,<sup>1</sup> Simen Kvaal,<sup>1</sup> Antoine Camper,<sup>2</sup> and Thomas Bondo Pedersen<sup>1</sup>

<sup>1</sup>*Hylleraas Centre for Quantum Molecular Sciences, Department of Chemistry, University of Oslo, P.O. Box 1033 Blindern, N-0315 Oslo, Norway*

<sup>2</sup>*Department of Physics, University of Oslo, P.O. Box 1048 Blindern, N-0316 Oslo, Norway*

(\*Electronic mail: t.b.pedersen@kjemi.uio.no)

(\*Electronic mail: einar.aurbakken@kjemi.uio.no)

(Dated: 19 March 2026)

We present a computational study of the laser-driven quantum dynamics of positronium (Ps), PsH, and PsCl at the time-dependent Hartree-Fock level of theory. To eliminate finite-basis effects and to properly capture continuum dynamics, we use a spherical polar pseudospectral representation. The multicomponent theory and its implementation are described in detail. We find that while the presence of the positron delays electron ionization in PsH, a slight enhancement of electron ionization is observed in PsCl. In both cases, the positronic response is faster than that of the electrons. We propose that the formation of PsCl may be directly observed through photopositron spectra in the multiphoton regime, where PsCl peaks are expected at roughly twice the energy of Ps peaks, making PsCl clearly distinguishable from Ps. In the tunnelling regime, however, photopositron rescattering peaks may only be distinguishable if the amount of Ps is sufficiently low.

## I. INTRODUCTION

When an electron comes into contact with its antiparticle, the positron, the pair decays into (typically) two gamma photons at 511 keV each. This quantum electrodynamical positron annihilation process is crucial for medical diagnostics through positron emission tomography and its recent extension to positronium imaging (PI).<sup>1–3</sup> The PI technique exploits the formation of short-lived positronium (Ps) “atoms”, the hydrogen-like state of a positron and an electron bound by their Coulomb interaction, inside the body. The key feature exploited for imaging is the strong dependence of the lifetime on the surroundings of Ps. Similarly, positron annihilation lifetime spectroscopy has evolved into an important characterization technique in chemistry and material science.<sup>2,4–8</sup>

Despite the advanced medical and scientific applications of positron annihilation, the bound states formed by positrons and atoms or molecules have proven very challenging to study theoretically. This poses a problem for further development of positron-based technologies and for fundamental scientific investigations of, e.g., exotic positron-mediated chemical bonding.<sup>9–12</sup> The main obstacle is the high-level many-body theory required to accurately describe electronic and electron-positron correlations and to predict positron affinities of atoms and molecules.<sup>13–16</sup> Experimentally, molecular positron affinities can be measured indirectly through vibrational Feshbach resonances<sup>17,18</sup> while alternative techniques have been proposed for atoms.<sup>19,20</sup> However, with lifetimes on the order of nanoseconds, it should be possible to study positron-matter binding and dynamics directly by ultrafast spectroscopy.

The development of femtosecond and attosecond laser pulses and associated technologies have paved the way for new research fields in chemistry and physics.<sup>21–23</sup> Different effects including impulsive stimulated scattering<sup>24</sup> have been discovered and new spectroscopic methods such as time-resolved pump-probe techniques have been developed. In addition, generation of strong-field pulses have revealed a

plethora of ultrafast strong-field phenomena such as non-sequential double ionization,<sup>25,26</sup> recollision-driven inner-shell processes,<sup>27</sup> emergence of plateaus in above-threshold ionization,<sup>28</sup> laser-induced electron diffraction,<sup>29</sup> and high-order harmonic generation.<sup>30,31</sup> These phenomena are generally well-described in the strong-field approximation<sup>32</sup> and have given birth to the field of attochemistry.<sup>33</sup> Laser-driven recollision processes have also been proposed for driving fusion<sup>34</sup> in clusters and for muon pair creation in Ps.<sup>35</sup>

In principle, laser interaction with positron binding atoms and molecules should also entail a large variety of ultrafast phenomena resembling the ones mentioned above, albeit with major differences due to the presence of the bound positron. The positron, located further out, will have a shielding effect on the electrons, altering the electron dynamics relative to the atomic or ionic counterpart system. Also, the positron itself will entail its own dynamics. One possibility for the positron is to tunnel ionize through the Coulombic potential and play the role of the rescattering particle. However, the numerical study of these phenomena is so far limited by the existing computational tools.

In 2018, Suzuki, Hagiwara, and Watanabe<sup>36</sup> reported an implementation of multicomponent time-dependent density-functional theory for coupled electron-positron dynamics driven by a laser field. Using a plane-wave basis with norm-conserving pseudopotentials, they presented an application to  $e^+ - \text{LiH}$  exposed to weak gaussian-shaped laser pulses with a peak intensity of  $0.53 \times 10^{12} \text{ W/cm}^2$  (electric-field strength  $0.2 \text{ V/\AA}$ ) and wavelengths of 413, 827, and 2480 nm (frequencies 0.5, 1.5, and 3.0 eV), showing that the presence of the positron suppresses a bound electronic excitation in LiH. Moreover, they found that the quivering motion of the electron density in  $e^+ - \text{LiH}$  is opposite to that in LiH. These effects were ascribed to dynamical electron-positron correlation.

Here, we neglect dynamical correlation and use all-particle grid-based time-dependent Hartree-Fock (TDHF) theory to shed light on the time evolution of positronium chloride (PsCl) exposed to external laser fields. Although the tar-

get quantity of interest in most ground-state studies, namely the positron binding energy, requires a high-level treatment of correlation effects (including large basis-set expansions) to achieve sufficient accuracy, the recent work by L ev eque-Simon *et al.*<sup>37</sup> indicates that the PsCl orbitals are qualitatively correct at the Hartree-Fock level. Extending this observation, we thus implicitly assume that the laser-induced quantum dynamics can be captured qualitatively correctly at the TDHF level of theory. Importantly, we effectively eliminate the basis-set issue,<sup>38,39</sup> both in the ground state and for the dynamical evolution of the wavefunction, by using a pseudospectral radial grid and angular expansions in spherical harmonics. Thus, high angular momenta are still needed for a proper description of the time-dependent wave function of systems subject to strong laser fields as well as for describing the ground state if correlated methods are employed, see, for example, the works by Saito.<sup>40,41</sup> The present work lays the foundations for correlated treatments using grid-based methodologies.

In this paper, we give a detailed account of TDHF theory for two-component systems in a spherical polar pseudospectral representation, including an exhaustive description of the integrator used to propagate the nonlinear TDHF equations. Rather than the density matrix, we focus on orbital time evolution to facilitate future extensions to correlated methods. Qualitative aspects of the laser-induced coupled electron-positron dynamics are discussed and related to the work of Suzuki, Hagiwara, and Watanabe.<sup>36</sup> We compute above-threshold ionization (ATI) spectra for the positron in both the multiphoton regime and in the tunneling regime, thus indicating a potential ultrafast spectroscopic method to detect PsCl. Finally, we compare TDHF results with those obtained from a ‘‘single active positron’’ (SAP) model where the electronic density is kept frozen at its ground-state distribution during the laser-driven dynamics. The SAP model thus is similar to the single active electron (SAE)<sup>42–44</sup> models that are widely used to study ultrafast laser-induced processes in electronic systems.

## II. THEORY

### A. Model and computational method

Unless stated otherwise, we use atomic units (a.u.) throughout this paper. The clamped-nuclei Born-Oppenheimer Hamiltonian<sup>45,46</sup> in a.u. of  $N_e$  electrons (mass 1 a.u., charge  $-1$  a.u.) and a single positron (mass 1 a.u., charge 1 a.u.) interacting with a time-dependent uniform electric field is given by

$$\hat{H} = \hat{h}^p(\mathbf{r}_p, t) + \sum_{i=1}^{N_e} \hat{h}^e(\mathbf{r}_i, t) + \sum_{i < j} \frac{1}{|\mathbf{r}_i - \mathbf{r}_j|} - \sum_{i=1}^{N_e} \frac{1}{|\mathbf{r}_p - \mathbf{r}_i|}, \quad (1)$$

with  $\mathbf{r}_i$  ( $\mathbf{r}_j$ ) and  $\mathbf{r}_p$  being the spatial coordinates of the  $i$ th ( $j$ )th electron and the positron, respectively. The term  $1/|\mathbf{r}_i - \mathbf{r}_j|$

is the *repulsive* Coulomb interaction between the  $i$ th and  $j$ th electrons, while  $-1/|\mathbf{r}_p - \mathbf{r}_i|$  is the *attractive* Coulomb interaction between the positron and the  $i$ th electron.

Within the velocity-gauge electric-dipole approximation, the single-electron and single-positron contributions to the Hamiltonian are given by

$$\hat{h}^e(\mathbf{r}, t) = -\frac{1}{2}\nabla^2 - V_{\text{ext}}(\mathbf{r}) - iA(t)\mathbf{u} \cdot \nabla, \quad (2)$$

$$\hat{h}^p(\mathbf{r}_p, t) = -\frac{1}{2}\nabla_p^2 + V_{\text{ext}}(\mathbf{r}_p) + iA(t)\mathbf{u} \cdot \nabla_p, \quad (3)$$

where

$$V_{\text{ext}}(\mathbf{r}) = \sum_{\alpha=1}^M \frac{Z_\alpha}{|\mathbf{r} - \mathbf{R}_\alpha|}, \quad (4)$$

is the potential due to  $M$  nuclei situated at  $\{\mathbf{R}_\alpha\}_{\alpha=1}^M$  with charge  $\{Z_\alpha\}_{\alpha=1}^M$ . For PsCl we have  $N_e = 18$ ,  $M = 1$ ,  $Z_{\text{Cl}} = 17$ , and  $\mathbf{R}_{\text{Cl}} = \mathbf{0}$ , while for PsH we have  $N_e = 2$ ,  $M = 1$ ,  $Z_{\text{H}} = 1$ , and  $\mathbf{R}_{\text{H}} = \mathbf{0}$ .

The linearly polarized vector potential  $A(t)\mathbf{u}$ , where  $\mathbf{u}$  is a real unit polarization vector, is related to the electric-field amplitude  $\mathcal{E}(t)$  as

$$A(t) = -\int_0^t \mathcal{E}(t') dt', \quad (5)$$

where we have assumed  $\mathcal{E}(0) = 0$ .

In the Hartree-Fock approximation (with the presence of a *single* positron), the wavefunction is the tensor product of a single  $N_e$ -electron Slater determinant and a single positron orbital<sup>47,48</sup>

$$\Psi(\mathbf{r}_1, \dots, \mathbf{r}_{N_e}, \mathbf{r}_p, t) = \Phi(\mathbf{r}_1, \dots, \mathbf{r}_{N_e}, t) \otimes \psi(\mathbf{r}_p, t). \quad (6)$$

We assume that the electron orbitals are doubly occupied—i.e., we use closed-shell spin-restricted Hartree-Fock (RHF) theory—such that the number of spatial orbitals is  $N_e/2$ .

The orbital equations of motion are derived using the stationary-action time-dependent variational principle. With the canonical gauge choice, the equations of motion for the time-dependent electron orbitals  $\{\phi_i(\mathbf{r}, t)\}_{i=1}^{N_e/2}$  and the positron orbital  $\psi(\mathbf{r}_p, t)$  become the (canonical) TDHF equations

$$i\partial_t \phi_i(\mathbf{r}, t) = \hat{f}^e(\{\phi_i\}, \psi, t) \phi_i(\mathbf{r}, t), \quad (7)$$

$$i\partial_t \psi(\mathbf{r}_p, t) = \hat{f}^p(\{\phi_i\}, \psi, t) \psi(\mathbf{r}_p, t). \quad (8)$$

The electron and positron Fock operators  $\hat{f}^e$  and  $\hat{f}^p$  are given by

$$\begin{aligned} \hat{f}^e(\{\phi_i\}, \psi, t) \phi_i(\mathbf{r}, t) &= \hat{h}^e(\mathbf{r}, t) \phi_i(\mathbf{r}, t) \\ &+ (2V^{\text{dir},e}(\mathbf{r}, t) - V^{\text{dir},p}(\mathbf{r}, t)) \phi_i(\mathbf{r}, t) \\ &- \sum_{j=1}^{N_e/2} V_{j,i}^{\text{exc},e}(\mathbf{r}, t) \phi_j(\mathbf{r}, t), \end{aligned} \quad (9)$$

$$\hat{f}^p(\{\phi_i\}, \psi, t) \psi(\mathbf{r}_p, t) = (\hat{h}^p(\mathbf{r}_p, t) - 2V^{\text{dir},e}(\mathbf{r}, t)) \psi(\mathbf{r}_p, t), \quad (10)$$

where we have introduced the direct and exchange potentials

$$V^{\text{dir},e}(\mathbf{r},t) = \sum_{j=1}^{N_e/2} \int \frac{|\phi_j(\mathbf{r}',t)|^2}{|\mathbf{r}-\mathbf{r}'|} d\mathbf{r}', \quad (11)$$

$$V^{\text{dir},p}(\mathbf{r},t) = \int \frac{|\psi(\mathbf{r}_p,t)|^2}{|\mathbf{r}-\mathbf{r}_p|} d\mathbf{r}_p, \quad (12)$$

$$V_{j,i}^{\text{exc},e}(\mathbf{r},t) = \int \frac{\phi_j^*(\mathbf{r}',t)\phi_i(\mathbf{r}',t)}{|\mathbf{r}-\mathbf{r}'|} d\mathbf{r}'. \quad (13)$$

The initial state is taken as the RHF ground state determinant of the field-free Hamiltonian ( $\mathcal{E}(t) = 0$ ), which is found by solving the stationary canonical RHF equations

$$\hat{f}^e(\{\phi_i\}, \psi, t=0)\phi_i(\mathbf{r}) = \varepsilon_i^e \phi_i(\mathbf{r}), \quad (14)$$

$$\hat{f}^p(\{\phi_i\}, \psi, t=0)\psi(\mathbf{r}_p) = \varepsilon_0^p \psi(\mathbf{r}_p), \quad (15)$$

for the occupied electron and positron orbitals.

In the absence of an external electric field, the Hartree-Fock potential (direct plus exchange) for atoms or ions with closed subshells (such as  $\text{Cl}^-$ ) is spherically symmetric.<sup>49</sup> This also holds for the direct potential due to the positron. Hence, to solve the HF equations for the initial state, we use spherical coordinates and assume that the orbitals are angular-momentum eigenfunctions of the form

$$\phi_i(r, \theta, \varphi) = r^{-1} u_{n,l}^i(r) Y_{l,m}(\theta, \varphi), \quad (16)$$

$$\psi(r, \theta, \varphi) = r^{-1} v_{n,l}(r) Y_{l,m}(\theta, \varphi). \quad (17)$$

For a linearly polarized electric field, the total potential becomes cylindrically symmetric and taking the polarization direction parallel to the  $z$ -axis, the interaction of the electrons or positron with the electric field can, in spherical coordinates, be written as

$$V(r, \theta, \varphi, t) = iqA(t) \left[ \cos\theta \frac{\partial}{\partial r} - \frac{\sin\theta}{r} \frac{\partial}{\partial \theta} \right]. \quad (18)$$

With this polarization, the initial quantum numbers  $m$  of the electron and positron orbitals are conserved,<sup>50</sup> and a time-dependent orbital can be expanded as

$$\phi_i(r, \theta, \varphi, t) = \sum_{l=0}^{l_{\max}} r^{-1} u_{l,m_i}^i(r,t) Y_{l,m_i}(\theta, \varphi), \quad (19)$$

$$\psi(r, \theta, \varphi, t) = \sum_{l=0}^{l_{\max}} r^{-1} v_{l,0}(r,t) Y_{l,0}(\theta, \varphi), \quad (20)$$

where  $l_{\max}$  is a finite cut-off value for the number of angular momenta included in the expansion. As each orbital has fixed  $m$ , we will in the following use the short-hand notation  $u_l^i(r,t) = u_{l,m_i}^i(r,t)$  and  $v_l(r,t) = v_{l,0}(r,t)$ . We note that the radial functions satisfy homogeneous Dirichlet boundary conditions, i.e.,  $u_{l,m}^i(r,t)$  and  $v_{l,0}(r,t)$  vanish at  $r=0$  and as  $r \rightarrow \infty$  for all  $t$ .

For the Coulomb interaction operator, we employ the multipole expansion<sup>49</sup>

$$\frac{1}{|\mathbf{r}_1 - \mathbf{r}_2|} \approx \sum_{L=0}^{L_{\max}} \sum_{M=-L}^L \frac{4\pi}{2L+1} \frac{r_{<}^L}{r_{>}^{L+1}} Y_{L,M}^*(\Omega_1) Y_{L,M}(\Omega_2), \quad (21)$$

where  $\Omega_i = (\theta_i, \varphi_i)$ ,  $i = 1, 2$ ,

$$r_{<} = \min(r_1, r_2), \quad r_{>} = \max(r_1, r_2), \quad (22)$$

and  $L_{\max}$  is a finite cut-off value.

Insertion of the above expansions into the TDHF equations and integrating out angular variables results in equations of motion for the radial part of the electron orbitals

$$\begin{aligned} i\partial_t u_l^i(r,t) &= -\frac{1}{2} \Delta_l u_l^i(r,t) - \frac{Z}{r} u_l^i(r,t) \\ &\quad - iA(t) [a_{l-1,m_i} D_{-l} u_{l-1}^i(r,t) + a_{l,m_i} D_{l+1} u_{l+1}^i(r,t)] \\ &\quad + 2 \sum_{l'} \mathfrak{D}_{l,l'}^{m_i}(r) u_{l'}^i(r,t) - \sum_{l'} \mathfrak{P}_{l,l'}^{m_i}(r) u_{l'}^i(r,t) \\ &\quad - \sum_j \sum_{l'} \mathfrak{X}_{ij,l,l'}^{m_i m_j}(r) u_{l'}^j(r,t), \end{aligned} \quad (23)$$

and the positron orbital

$$\begin{aligned} i\partial_t v_l(r,t) &= -\frac{1}{2} \Delta_l v_l(r,t) + \frac{Z}{r} v_l(r,t) \\ &\quad + iA(t) [a_{l-1,0} D_{-l} v_{l-1}(r,t) + a_{l,0} D_{l+1} v_{l+1}(r,t)] \\ &\quad - 2 \sum_{l'} \mathfrak{D}_{l,l'}^0(r) v_{l'}(r,t). \end{aligned} \quad (24)$$

Here, we have used the following definitions

$$a_{l,m} = \sqrt{\frac{(l+1)^2 - m^2}{(2l+1)(2l+3)}}, \quad (25)$$

$$D_l = \frac{\partial}{\partial r} + \frac{l}{r}, \quad (26)$$

$$\Delta_l = \frac{\partial^2}{\partial r^2} - \frac{l(l+1)}{r^2}. \quad (27)$$

The radial forms of the direct and exchange matrices are

$$\mathfrak{D}_{l,l'}^{m_i}(r) = \sum_j \sum_L \sum_{l_1 l_2} u_{l_1 l_2, L}^{j,j}(r) g_{l_1 l_2}^{m_i m_j} g_{l l'}^{m_i m_i}, \quad (28)$$

$$\mathfrak{P}_{l,l'}^{m_i}(r) = \sum_L \sum_{l_1 l_2} v_{l_1 l_2, L}(r) g_{l_1 l_2}^{00} g_{l l'}^{m_i m_i}, \quad (29)$$

$$\mathfrak{X}_{ij,l,l'}^{m_i m_j}(r) = \sum_L \sum_{l_1 l_2} u_{l_1 l_2, L}^{j,i}(r) g_{l_1 l_2}^{m_j m_i} g_{l l'}^{m_i m_j} (-1)^{m_j - m_i}, \quad (30)$$

where we have defined the radial components of the direct and exchange potentials as

$$u_{l_1 l_2, L}^{j,i}(r) = \frac{4\pi}{2L+1} \int \frac{r_{<}^L}{r_{>}^{L+1}} u_{l_1}^{j,*}(r') u_{l_2}^i(r') dr', \quad (31)$$

$$v_{l_1 l_2, L}(r) = \frac{4\pi}{2L+1} \int \frac{r_{<}^L}{r_{>}^{L+1}} v_{l_1}^*(r') v_{l_2}(r') dr', \quad (32)$$

and an array of Gaunt-like coefficients

$$g_{l_1 l_2}^{m_i m_j} = \int Y_{l_1, m_i}^*(\Omega) Y_{L, (m_i - m_j)}(\Omega) Y_{l_2, m_j}(\Omega) d\Omega. \quad (33)$$

The radial coordinate is discretized using the Gauss-Legendre-Lobatto (GLL) pseudospectral method (see Appendix A), and the ground-state RHF equations are solved numerically following the procedure described in Ref. 51.

The radial direct and exchange potentials (Eqs. (31) and (32)) satisfy a Poisson equation, which is solved on the GLL grid following the procedure in Ref. 52. In principle, one could have computed the direct and exchange potentials by quadrature. However, due to presence of the derivative singularity at  $r = r'$ , superior numerical accuracy is achieved by solving the Poisson equation.<sup>52</sup>

For the time propagation, we use the approximate second-order constant density matrix (CDM2) integration scheme described in detail in Appendix B.

The electric-field amplitude, representing a laser pulse with carrier frequency  $\omega$  and zero carrier-envelope phase, is modeled by a sine-wave modulated by a trigonometric envelope function<sup>53</sup>

$$\mathcal{E}(t) = \mathcal{E}_0 \sin^2\left(\pi \frac{t}{t_d}\right) \sin(\omega t), \quad 0 \leq t \leq t_d, \quad (34)$$

where  $\mathcal{E}_0$  is the maximum field strength such that the peak intensity is given by  $(1/2)\epsilon_0 c \mathcal{E}_0^2$ , and  $t_d$  is the (foot-to-foot) duration of the laser pulse. All simulations are done in velocity gauge with the vector potential obtained from the electric field according to Eq. (5). The electric field is turned on at  $t = 0$  and turned off after  $t_d = n_c t_c$ , where  $t_c = 2\pi/\omega$  is one optical cycle and  $n_c$  the number of optical cycles.

Finally, we will also do simulations of Ps. In this case we separate the two-particle Hamiltonian into a center-of-mass term, which does not couple to the electric field in the electric-dipole approximation, and an internal single-particle (hydrogen-like) Hamiltonian with the coordinate origin at the electron (i.e., we use the relative coordinate  $\mathbf{r} = \mathbf{r}_p - \mathbf{r}_e$ ) and with reduced mass  $\mu = 1/2$  and charge  $q = 1$ . The internal Hamiltonian for Ps in an external electric field thus is given by

$$\hat{H}_{\text{Ps}} = (\mathbf{p} - A(t)\mathbf{u})^2 - \frac{1}{r}. \quad (35)$$

The time-dependent Schrödinger equation for Ps is solved numerically using the same pseudo-spectral discretization as for the TDHF equations, with the wavefunction expansion in Eq. (20) and with the ground-state wavefunction as initial condition.

### B. Above-threshold ionization spectra

To investigate positron ionization we compute ATI spectra using the procedure proposed by Schafer and Kulander.<sup>43</sup> That is, we calculate expectation values of the operator

$$\hat{W}(E; \Gamma) = \frac{\Gamma^4}{(\hat{H} - E)^4 + \Gamma^4}, \quad (36)$$

in the final positronic state  $|\psi_f\rangle$  after interaction with the laser pulse such that the positron yield for an energy  $E$  is given by  $\langle \psi_f | \hat{W}(E; \Gamma) | \psi_f \rangle$ . Here,  $\Gamma$  is a broadening parameter and  $\hat{H}$  is the Hamiltonian whose expectation value gives the energy of the positron as  $t \rightarrow \infty$ . For PsCl,  $\hat{H}$  is the Fock operator for the positron, while for Ps we assume equal kinetic energies

of the electron and the positron after ionization and thus  $\hat{H} = \frac{1}{2}\hat{H}_{\text{Ps}}$ .

Since the yield for each energy in the generated spectrum is essentially a weighted sum of contributions from eigenstates of the Hamiltonian close in energy, the spectrum depends heavily on how well the eigenstates match the actual continuum states. If  $r_{\text{max}}$  is chosen too small, the ATI spectrum will appear noisy even though the simulation parameters are well converged. We deal with this in two ways. The first way is to increase the broadening parameter  $\Gamma$ , as the averaging of contributions from nearby states will ultimately remove the noise. However, this also reduces the resolution of the spectrum. The second way is to map the final wavefunction onto a larger grid prior to the energy analysis. We do this using barycentric polynomial interpolation.

## III. RESULTS

### A. Computational details

For the radial grids, we use  $N_r = 1.25r_{\text{max}}$  grid points in all simulations, as we have found this to be sufficient to get converged results. We minimize reflections by converging the simulations with respect to  $r_{\text{max}}$  and, in addition, we use a mask function of the form<sup>50</sup>

$$M(r) = \begin{cases} 1, & r < r_0 \\ \cos^{1/4}\left(\frac{\pi}{2} \frac{r - r_0}{r_{\text{max}} - r_0}\right), & r_0 \leq r < r_{\text{max}} \end{cases}, \quad (37)$$

where we choose  $r_0 = r_{\text{max}} - 30a_0$ . For the spherical expansions, we use odd values of  $l_{\text{max}}$ , and  $L_{\text{max}} = (l_{\text{max}} - 1)/2$ . Time steps are  $\Delta t = 0.1$  a.u. unless otherwise stated.

### B. Initial state

The ground state of PsCl is an S state (total angular momentum 0). In agreement with the results reported by Saito<sup>54</sup> for PsH using Hylleraas functions, the addition of a spherically symmetric attractive Coulomb potential from the positron squeezes the electrons toward the atomic nucleus. This effect, however, is much less pronounced for PsCl than for PsH, as can be seen in Fig. 1. The lower-level sub-shells are left out of the figure since the orbitals from PsCl and  $\text{Cl}^-$  are indistinguishable at this scale.

To quantify the effect of the positron on the electronic orbitals, we define the orbital relaxation energy

$$\Delta E_{\text{PsA}}^{\text{relax}} = E_{\text{Ps-A}} - E_{\text{PsA}}^{\text{HF}}, \quad (38)$$

along with the relative orbital relaxation energy,

$$\delta E_{\text{PsA}}^{\text{relax}} = \frac{\Delta E_{\text{PsA}}^{\text{relax}}}{E_{\text{PsA}}^{\text{HF}}}, \quad (39)$$

where  $E_{\text{PsA}}^{\text{HF}}$  is the full self-consistent HF energy of PsA, while  $E_{\text{Ps-A}}$  is obtained by diagonalizing  $\hat{f}^p$  in the mean-field of

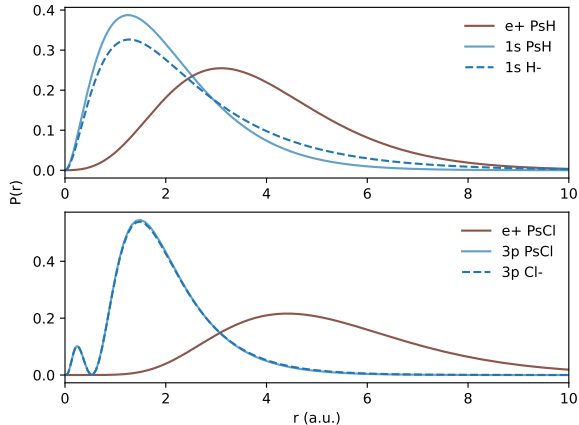


FIG. 1. Radial distribution functions for the positron orbital and the outermost electron orbitals of PsH (top) and PsCl (bottom).

$A^-$  and creating a product state of the  $A^-$  ground-state Slater determinant and the resulting positron orbital.

We find  $\Delta E_{\text{PsH}}^{\text{relax}} = 14 \text{ mE}_h$  and  $\Delta E_{\text{PsCl}}^{\text{relax}} = 1.2 \text{ mE}_h$ , while the relative values are  $\delta E_{\text{PsH}}^{\text{relax}} = 2.1\%$  and  $\delta E_{\text{PsCl}}^{\text{relax}} = 2.5 \times 10^{-4}\%$ . This confirms that the effect of the positron is much smaller on the electrons in PsCl than in PsH, not just in relative terms but also in absolute terms. At least in the mean-field model, the addition of the positron to  $\text{Cl}^-$  constitutes a small perturbation of the electronic system.

### C. Qualitative assessment of the dynamics

Although the addition of a positron to  $\text{Cl}^-$  has little effect on the ground-state electronic orbitals, the situation is markedly different for laser-induced dynamics. Because of the addition of a light positive charge, the dynamics in PsA systems are more complex than in ordinary atoms. The electrons are bound to a central attractive potential, whereas the positron is bound only due to the presence of the electrons. This breaks the symmetry between the electron and the positron present in isolated Ps.

According to Ehrenfest's theorem<sup>55</sup>

$$\frac{d^2}{dt^2} \langle \hat{z} \rangle = q \mathcal{E}(t) - \left\langle \frac{\partial V}{\partial \hat{z}} \right\rangle, \quad (40)$$

where  $\hat{z}$  is the position operator of either the electrons ( $q = -1$ ) or the positron ( $q = +1$ ) and  $V$  denotes the total Coulomb operator, the laser-induced dynamics become a balance of forces stemming from the external laser field and the attractive mean-field Coulomb forces among the electrons and the positron. Suzuki, Hagiwara, and Watanabe<sup>36</sup> noted that in the  $e^+ \text{-LiH}$  system, the electron moves in the same direction as the external field, opposite to what is expected from the first term in Eq. (40). For weak, low-frequency pulses, we observe exactly the same in PsCl, as illustrated by the top panel in Fig. 2. The fundamental reason for this is that the positron

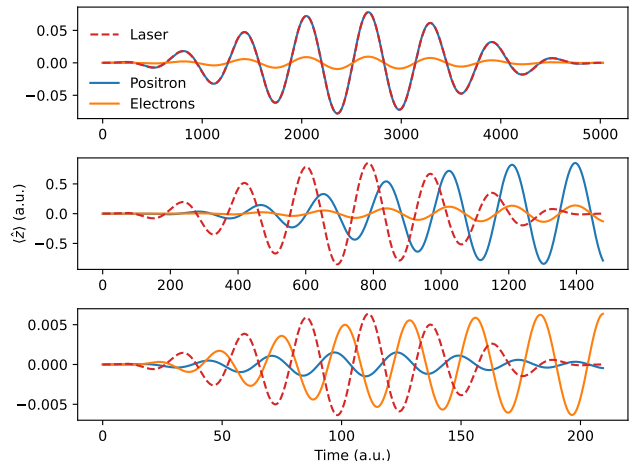


FIG. 2. Position expectation value for electrons and positron in PsCl subject to a weak ( $\mathcal{E}_0 = 0.0001 \text{ a.u.}$ ) 8-cycle laser pulse with frequencies 0.01 a.u. (top), 0.034 a.u. (middle) and 0.24 a.u. (bottom). These correspond, in order, to a frequency in the transparent region, the first positron resonance, and the first electronic resonance. The units of the laser pulse are arbitrary, as its meant to show the phase between the electric field and the position expectation values. The grid parameters were  $r_{\text{max}} = 100$  and  $l_{\text{max}} = 9$ .

is more loosely bound than the electrons and consequently exhibits a stronger response to the external field. The attractive electrostatic field set up by the displaced positron locally dominates the potential due to the laser field, essentially making the electrons follow the motion of the positron. Fig. 3 shows a snapshot of this effect at  $t = 2600 \text{ a.u.}$  for the run corresponding to the top panel in Fig. 2, but with field strength increased to  $\mathcal{E}_0 = 0.001 \text{ a.u.}$  to make the effect more easily visible on the figure.

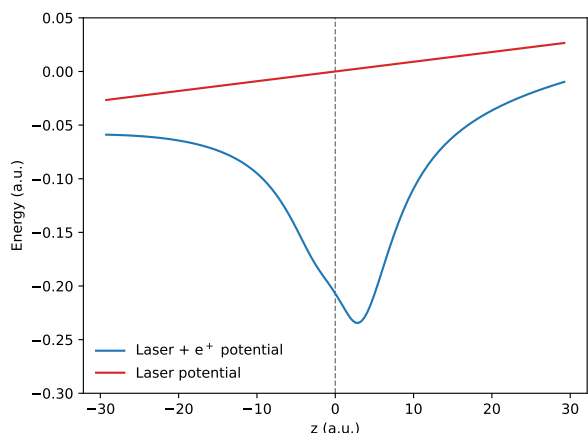


FIG. 3. The external potential (excluding nucleus) seen by the electrons in a  $\text{Cl}^-$  system with and without a positron.

While the external laser field pushes the electrons to the right, the total external potential (the sum of the external laser

field and the electrostatic potential due to the positron) attracts them to a local minimum to the left.

For sufficiently weak and sufficiently long (i.e., roughly adiabatically switched-on) laser pulses, the change in the electronic and positronic position expectation value can be expressed in terms of stationary states  $|n\rangle$  and ground-to-excited state transition energies  $\omega_n$  as

$$\Delta\langle\hat{z}\rangle(t) \approx 2q^{-1} \sum_{n>0} \frac{\omega_n |\langle 0|\hat{z}|n\rangle|^2}{\omega_n^2 - \omega^2} \mathcal{E}_0 \sin(\omega t). \quad (41)$$

While this linear-response expression suggests that positrons should follow the field and electrons move oppositely in the transparent region  $\omega < \omega_1$ , it also indicates that the relative phase angle between the external laser field and the induced dipole moment shifts by  $180^\circ$  as the frequency passes through the first transition energy  $\omega_1$ . This typically happens in ordinary atoms, and we observe the same in the PsA systems. However, both the positron and the electrons go through separate resonant regimes, causing more complex dynamics.

For a closer examination of this phenomenon, we write the induced position expectation value as

$$\Delta\langle\hat{z}\rangle(t) \sim G(t) \sin(\omega t - \theta), \quad (42)$$

where  $G(t)$  varies on a longer time scale than the sine function. This expression gives an approximate definition of the relative phase angle,  $\theta$ , between the external laser field defined in Eq. (34) and the induced dipole moment. In practice,  $\langle\hat{z}\rangle$  is obtained from the simulation and we calculate the phase angles approximately following the steps in Appendix C.

Figure 4 shows the relative phase angle between the maximum laser peak in a weak ( $\mathcal{E}_0 = 0.0001$  a.u.) 8-cycle pulse and the corresponding peaks in the dipole moment of the electrons and the positron. This figure also includes the corresponding dipole moments from two reference simulations: the SAP model and a model in which the positron is kept frozen.

As the frequency approaches the first positronic resonance, the electron and positron oscillation remains in sync. The dynamics are dominated by the positron, although the electronic dynamics have a small effect on the energy at which the phase shift occurs. As we reach the first electronic resonance, the roles reverse in the sense that the energy transfer to the electronic system is so large that the electronic dynamics dominate the positron dynamics. This can be seen from the fact that the electronic phase angle is almost identical to the one in the frozen positron simulation, while the positron phase angle deviates substantially from the frozen electron simulation. As seen in the bottom panel of Fig. 2, the magnitude of the dipole moment is substantially greater for the electrons than for the positron in this region.

The discussion so far has been concerned with bound dynamics, but also the ionization dynamics exhibit interesting features. Figure 5 shows the ionization density for the positron and electrons in PsH and PsCl subjected to a laser field with parameters  $\omega = 0.02$  a.u., and field strengths  $\mathcal{E}_0 = 0.0123443$  a.u. for PsH and  $\text{H}^-$ , and  $\mathcal{E}_0 = 0.01073842$  a.u. for PsCl and  $\text{Cl}^-$ . For PsH, we observe sequential ionization, with the positron ionizing first, followed by the elec-

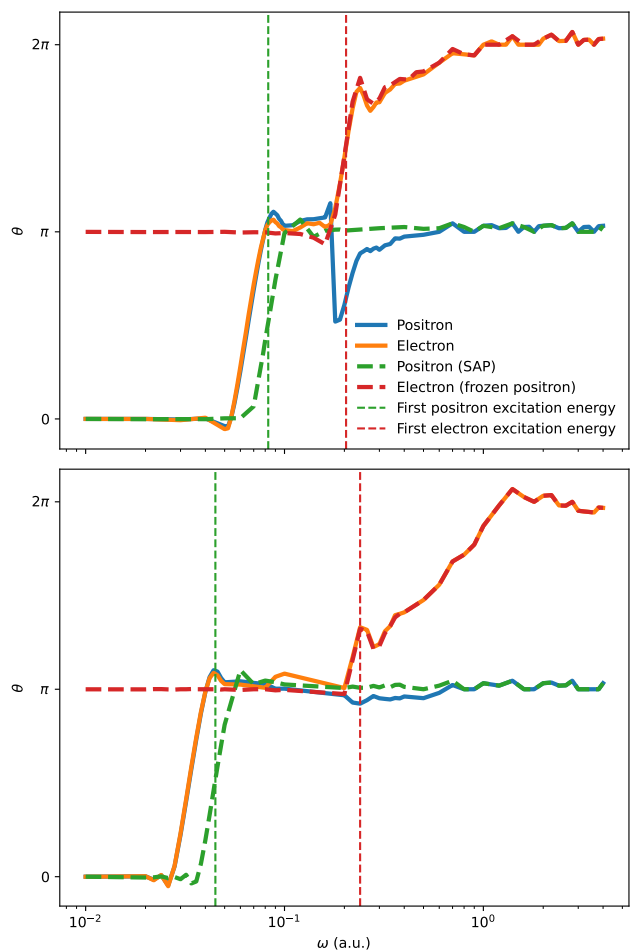


FIG. 4. The relative phase angle,  $\theta$ , between the laser field and  $\langle\hat{z}\rangle$  for the positron and electrons in PsH (top) and PsCl (bottom) as a function of the field frequency. A weak ( $\mathcal{E}_0 = 0.0001$  a.u.) 8-cycle laser pulse was applied.

tron. The electron ionization is substantially delayed compared with  $\text{H}^-$ . However, in PsCl the electron ionization is slightly enhanced compared to in  $\text{Cl}^-$  after the initial positron ionization—although, it should be noted that the electron ionization is three orders of magnitude smaller than the positron ionization in this case. It seems as if the positron dynamics induces more electron ionization than the external field itself, consistent with the creation of a small amount of positronium. Correlated wavefunction models would be required to confirm this. The positron-induced electron ionization is further supported by reference simulations holding the positron density fixed in the ground state, which quenches the electron ionization almost completely, to only about  $10^{-7}$  at the end of the simulation.

Figure 6 shows the difference between the electron and positron energy levels in the two pairs of systems. When the positron ionizes in PsH, the ionization potential for the electron is small, while in PsCl, it is about the same as for the positron. Conspicuously, the ionization of the positron in PsCl is much greater than the electron in  $\text{Cl}^-$ , despite the valence

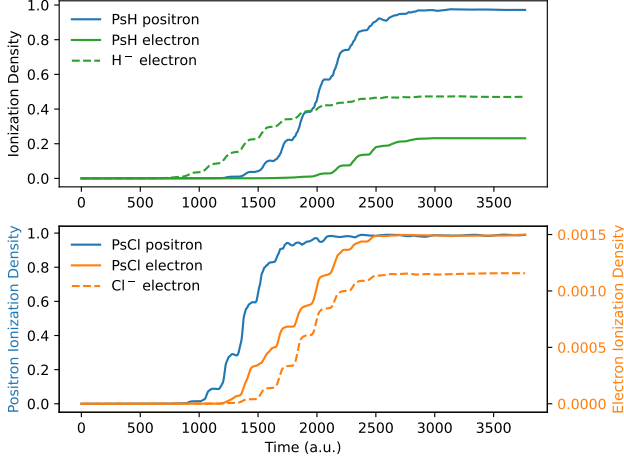


FIG. 5. Electron and positron ionization densities for PsH (top,  $\sim 5.35 \times 10^{12}$  W/cm<sup>2</sup>) and PsCl (bottom,  $\sim 4.05 \times 10^{12}$  W/cm<sup>2</sup>). We used a 12 cycle pulse with frequency 2280 nm. The grid parameters were  $r_{\max} = 175$  and  $l_{\max} = 23$ , and we used time step  $dt = 0.05$  a.u.

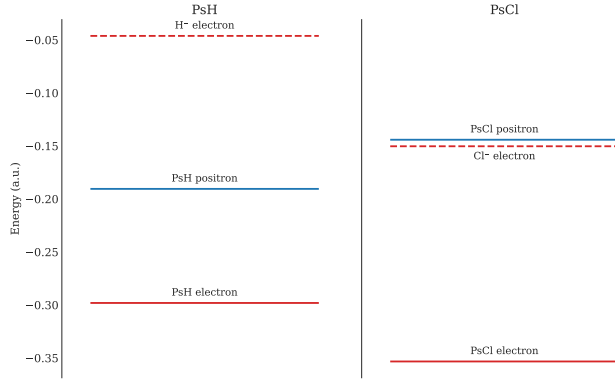


FIG. 6. Positron orbital energies and electron valence orbital energies for  $H^-$ ,  $Cl^-$ , PsH and PsCl.

orbital energies being almost the same. This is likely due to the differences in the shape of the effective potential seen by the different particles, as illustrated in Fig. 7.

#### D. ATI spectra of PsCl and Ps

Figure 8 shows ATI spectra for the positron of Ps and PsCl due to a 10-cycle laser pulse with  $\omega = 0.085645$  a.u. and  $\mathcal{E}_0 = 0.0068795$  a.u., which corresponds to a laser pulse with wavelength  $\lambda \sim 532$  nm and intensity  $I \sim 1.66 \times 10^{12}$  W/cm<sup>2</sup>. This corresponds to Keldysh parameter values of  $\gamma = 8.8$  and  $\gamma = 6.7$  for the Ps and PsCl systems, respectively, placing us firmly within the multiphoton regime for both systems. For the calculation of these spectra, we used  $r_{\max} = 1000$  and  $l_{\max} = L_{\max} = 5$ , which yields well converged results. Such a large radial grid is necessary since even the highest-energy (ionized) electrons must not have been absorbed by the mask function at the end of the pulse. We mapped the final state

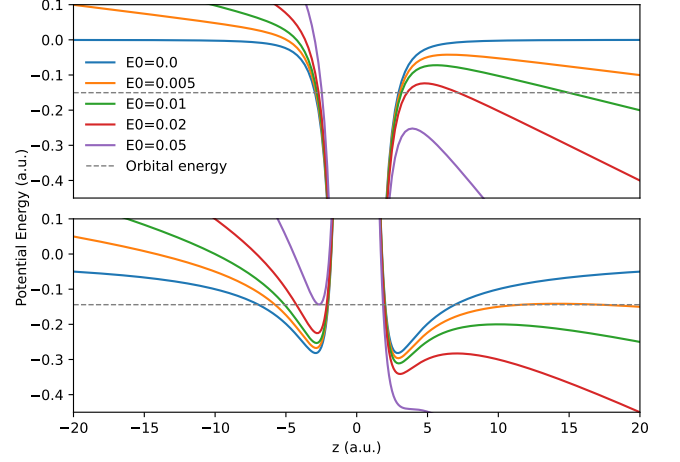


FIG. 7. Ground state mean-field potentials along the  $z$ -axis seen by the valence electron in  $Cl^-$  (top) and the positron in PsCl (bottom) at peak amplitude for various external field strengths. The orbital energy is for the valence electron (top) and positron (bottom).

onto a radial grid with  $r_{\max} = 7000$  for the energy analysis, and used a broadening parameter  $\Gamma = 0.0125$  eV.

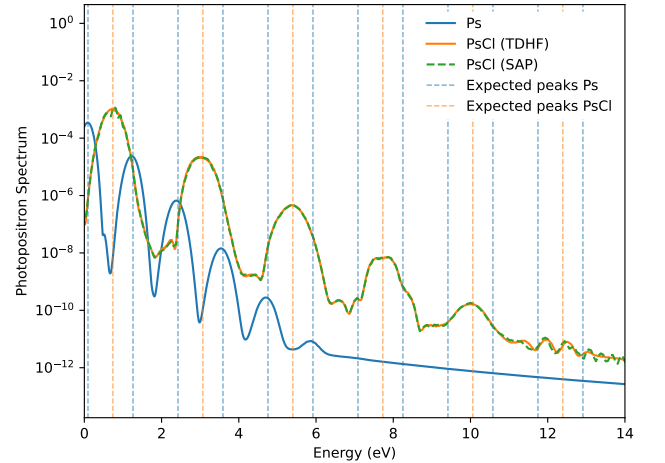


FIG. 8. Weak-field (10 cycles,  $\sim 1.66 \times 10^{12}$  W/cm<sup>2</sup>,  $\sim 532$  nm) photopositron spectrum for Ps and PsCl using the TDHF and SAP models.

Due to the symmetry between the electron and the positron in Ps, the distance between multiphoton ATI peaks is halved relative to an atom. This is because the kinetic energy gained by absorbing a photon is shared equally between the electron and the positron. In a positronium-binding atom, this symmetry is broken. In particular, the electrons are bound tighter around the nucleus in the ground state. The multiphoton ATI patterns can therefore be expected to look more similar to those in an atom. This indicates that if PsCl has been successfully produced experimentally, positron ATI peaks should appear at near twice the energy of that in pure Ps. We see in Fig. 8 that despite the substantial contributions of the elec-

tron potential, the ATI peaks are located as predicted from the positron orbital energy. Moreover, we note that highest-lying PsCl ATI peaks, above  $\sim 7$  eV, are well separated from the Ps peaks, potentially enabling direct spectroscopic identification of PsCl despite the presence (of relatively large amounts) of Ps. Since the positron binding energy is underestimated at the RHF level, including correlation in the simulation should shift the PsCl peaks somewhat down in energy. It is unlikely, however, that the shift is large enough to place the highest-lying PsCl peaks within the Ps spectrum.

The situation becomes somewhat different as we enter the tunneling regime. In this case, a plateau is expected to appear in the ATI spectra due to backscattering. This process, along with a theoretical cutoff for the maximal energy a particle can acquire, can be largely described classically using the “simpleman’s model”.<sup>56</sup> Energies that ionized electrons can obtain by various processes in different directions can be estimated in terms of the ponderomotive energy, which for an electron or positron is given by

$$U_p = \frac{\mathcal{E}_0^2}{4\omega^2}. \quad (43)$$

For an atom, the maximal energy the electron can obtain is roughly  $10U_p$ . If we replace the electron in the “simpleman’s model” with an electron-positron pair, the model predicts the maximal energy of each particle in Ps to be  $10U_p$ , giving the total system  $20U_p$  of energy. Thus, the cutoff energy for a positron in Ps is expected to be the same as in PsCl. This is seen in figure 9, which shows ATI spectra for Ps and PsCl after irradiation by a 4-cycle laser pulse with  $\omega = 0.057$  a.u. ( $\sim 800$  nm) and  $\mathcal{E}_0 = 0.053$  a.u. ( $\sim 9.86 \times 10^{13}$  W/cm<sup>2</sup>). These laser parameters correspond to  $\gamma = 0.76$  and  $\gamma = 0.57$  for Ps and PsCl, respectively. That is, we are within the tunneling regime.

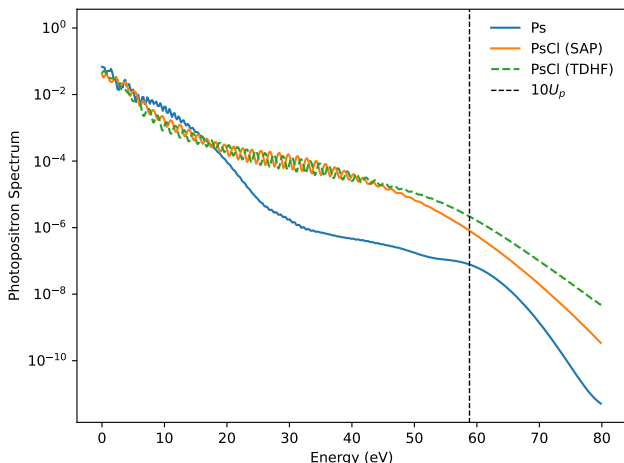


FIG. 9. Strong-field (4 cycles,  $\sim 9.86 \times 10^{13}$  W/cm<sup>2</sup>,  $\sim 800$  nm) photopositron spectrum for Ps and PsCl using the TDHF and SAP models. Broadening factor was 0.1 eV.

It is evident from Fig. 9 that the PsCl rescattering should be clearly visible in an experimental spectrum provided that the

amount of Ps present is sufficiently low. Although the peaks in the plateau would change, including electron and electron-positron correlations in the simulation is not expected to significantly alter this prediction.

Figures 8 and 9 also display the spectra obtained with the SAP model. The SAP model performs very well for PsCl in the multiphoton regime, producing an ATI spectrum virtually identical to that obtained with TDHF theory. Deviations between TDHF and SAP results are only observed at the highest energies from roughly 11 eV to 14 eV in Fig. 8. In the tunneling regime, however, the SAP model performs significantly worse due to stronger electronic response to the external laser, see Fig. 9. The cutoff energies observed with the SAP and TDHF models are in reasonable agreement, though.

#### IV. CONCLUDING REMARKS

We have presented a computational study of the coupled electron and positron dynamics driven by laser fields for Ps, PsH, and PsCl at the TDHF level of theory, using a spherical polar pseudospectral representation to eliminate finite-basis effects and to capture continuum dynamics. The methodology is described in detail, including an account of the approximate second-order integrator used to solve the TDHF equations of motion for both electronic and positronic degrees of freedom.

Investigating the “synchronization” of the electronic and positronic quiver motion along the direction of a weak external electric field observed in a previous work by Suzuki, Hagiwara, and Watanabe,<sup>36</sup> we have argued that it is caused by a shift in the effective potential minimum of the electrons due to the presence of the positron. The effect is frequency-dependent, however, and the relative motion of the electrons and the positron may align or anti-align.

For stronger laser pulses, we find that positron ionization is faster and stronger than electron ionization. Electron ionization is significantly delayed in PsH relative to the free H<sup>-</sup> ion, while a slight enhancement is observed in PsCl relative to Cl<sup>-</sup>. These observations may be altered, however, if electron and electron-positron correlations are included in the theoretical model.

We propose that photopositron spectra obtained with short laser pulses at 532 nm may be used to confirm the formation of PsCl using the (close to) doubling of the energy range of peaks in the multiphoton ionization regime. In strong-field cases at 800 nm (in the tunnelling regime), however, the expected plateau in the photopositron spectrum of PsCl will likely only be clearly distinguishable from Ps if its concentration is low enough. We argue that although the photopositron peaks (position and intensity) will likely change when correlations are included in the theoretical model, these observations will remain valid.

The essential next step to improve and confirm the overall results presented here will be to include electron and electron-positron correlation using the pseudospectral representation.

## Appendix A: The pseudospectral method

In this paper, single-particle functions are represented using polar coordinates. A partial wave expansion is employed, leading to a tensor product basis of spherical harmonics and radial basis functions. The radial functions are discretized with a pseudospectral method we now describe. In the pseudospectral method<sup>51,57</sup> a function  $f(\xi) : [-1, 1] \rightarrow \mathbb{C}$  is approximated as

$$f(\xi) \approx f_N(\xi) = \sum_{k=0}^N f(\xi_k) C_k(\xi), \quad (\text{A1})$$

where  $C_k(\xi)$  are the cardinal functions, in our case polynomials of degree  $N$  satisfying

$$C_k(\xi_j) = \delta_{jk}. \quad (\text{A2})$$

Thus, we have a global representation in terms of polynomials of degree  $N$ . The grid points can be chosen in numerous ways, often as nodes of a Gaussian quadrature rule, leading to highly efficient and accurate evaluation of variational matrix elements and rapid convergence of the polynomial expansion.

In a standard Gauss grid (or ‘‘roots grid’’), the grid points (abscissa) are the roots (zeros) of an associated orthogonal polynomial  $P_N(\xi)$  of order  $N$  (Legendre, Chebyshev, Hermite, Laguerre, etc.).

Alternatively, the grid points are taken as the roots ( $N - 1$ ) of the derivative of the associated polynomial plus two (specified) endpoints, which is referred to as a Lobatto grid. According to Boyd<sup>57</sup>, the Lobatto grid is favored for solving boundary value problems because boundary conditions determine two grid point values of the unknown  $f(\xi)$  (or  $f_N(\xi)$ ). Moreover, Lobatto grids can be combined with the finite-element method,<sup>58,59</sup> which can be exploited for increased efficiency and flexibility in the design of the grid.

Integrals over some domain are approximated by an associated Gaussian quadrature rule

$$\int f(\xi) d\xi \approx \sum_{k=0}^N f(\xi_k) w_k, \quad (\text{A3})$$

where  $w_k$  are the quadrature weights (see below).

The derivative of  $f(\xi)$  at a grid point  $\xi_j$  is approximated by the exact derivative of the polynomial interpolant,

$$f'(\xi_j) \approx \sum_k f(\xi_k) C'_k(\xi_j) = \sum_k D_{j,k}^{(1)} f(\xi_k), \quad (\text{A4})$$

where we have defined the first derivative matrix

$$D^{(1)} \equiv [D_{j,k}^{(1)}] \equiv [C'_k(\xi_j)], \quad (\text{A5})$$

which can be found analytically for certain polynomials such as Legendre and Chebyshev<sup>57</sup>.

If the function  $f(\xi)$  satisfies homogeneous Dirichlet boundary conditions

$$f(\xi_0) = 0, \quad f(\xi_N) = 0, \quad (\text{A6})$$

the second derivative matrix for  $i, j = 1, 2, \dots, N - 1$  is given by

$$D_{ij}^{(2)} = \sum_{k=1}^{N-1} D_{ik}^{(1)} D_{kj}^{(1)}. \quad (\text{A7})$$

### The Gauss-Legendre-Lobatto grid

In this work, we have used a Gauss-Legendre-Lobatto (GLL) grid where  $P_N(\xi)$ ,  $\xi \in [-1, 1]$  is the Legendre polynomial of order  $N$ . The inner grid points are the roots of  $P'_N(\xi)$

$$P'(\xi_k) = 0, \quad k = 1, 2, \dots, N, \quad (\text{A8})$$

and the endpoints are  $\xi_0 = -1$  and  $\xi_{N+1} = 1$ . The quadrature weights are given by

$$w_k = \frac{2}{N(N+1)P_N(\xi_k)^2}. \quad (\text{A9})$$

The grid points and weights can be determined numerically using, for example, as we have done, the `polynomial`<sup>60</sup> package in NumPy.

Furthermore, the matrix elements of the differentiation operator can be found analytically, see, for example Refs. 51, 57<sup>61</sup>

$$D_{ij}^{(1)} \equiv \left. \frac{dC_j}{d\xi} \right|_{\xi=\xi_i} = C'_j(\xi_i) = \tilde{C}'_j(\xi_i) \frac{P_N(\xi_i)}{P_N(\xi_j)}, \quad (\text{A10})$$

$$\tilde{C}'_j(\xi_i) = \begin{cases} -\frac{1}{4}N(N+1) & i = j = 0, \\ \frac{1}{4}N(N+1) & i = j = N, \\ 0 & i = j \text{ and } 1 \leq j \leq N-1, \\ \frac{1}{\xi_i - \xi_j} & i \neq j. \end{cases} \quad (\text{A11})$$

### Change of interval

Since we work in spherical coordinates, the GLL grid points have to be mapped from  $[-1, 1] \rightarrow [0, r_{\max}]$ . We have used the linear mapping

$$r(\xi) = \frac{r_{\max}}{2} (\xi + 1). \quad (\text{A12})$$

Integrals are then given by

$$\begin{aligned} \int_0^{r_{\max}} f(r) dr &= \int_{-1}^1 f(r(\xi)) \dot{r}(\xi) d\xi \\ &= \sum_k \dot{r}(\xi_k) f(r(\xi_k)) w_k, \end{aligned} \quad (\text{A13})$$

where

$$\dot{r}(\xi) \equiv \frac{dr}{d\xi}, \quad (\text{A14})$$

which for the linear mapping (A12) is constant and given by

$$\dot{r}(\xi) = \frac{r_{\max}}{2}. \quad (\text{A15})$$

We stress that, as discussed in section II A, the radial components of the direct and exchange potentials defined by Eqs. (31) and (32) are *not* computed by the quadrature formula (A13), but are instead found by solving an associated Poisson equation.

To express the time-dependent radial TDHF equations of motion (23) and (24) in the pseudospectral basis one needs to relate the first and second derivative of a function  $f(r)$  with respect to  $r$  to the variable  $\xi$ . By the chain rule we obtain

$$\frac{df(r)}{dr} = \frac{1}{\dot{r}(\xi)} \frac{df}{d\xi}, \quad (\text{A16})$$

$$\frac{d^2f(r)}{dr^2} = \frac{1}{\dot{r}(\xi)^2} \frac{d^2f}{d\xi^2} - \frac{\ddot{r}(\xi)}{\dot{r}(\xi)^3} \frac{df}{d\xi}, \quad (\text{A17})$$

where the second term in the double derivative vanishes for the linear mapping since  $\ddot{r}(\xi) = 0$ .

## Appendix B: Time integration

### 1. The TDHF equations on matrix form

We now indicate how the TDHF equations are written as a *non-linear* matrix equation. Here, we consider the electronic (restricted) TDHF equation for the occupied orbitals ( $i = 1, \dots, N_e/2$ ) given by

$$i|\dot{\phi}_i(t)\rangle = (\hat{h}(t) + \hat{v}^{\text{RHF}})|\phi_i(t)\rangle, \quad (\text{B1})$$

where

$$\hat{v}^{\text{RHF}}|\phi_i\rangle = 2 \sum_{j=1}^{N_e/2} \langle \phi_j | \phi_i \phi_j \rangle - \sum_{j=1}^{N_e/2} \langle \phi_j | \phi_j \phi_i \rangle. \quad (\text{B2})$$

Here, we have defined

$$\langle \phi_j | \phi_k \phi_l \rangle \equiv \left( \int \frac{\phi_j^*(\mathbf{r}_2) \phi_l(\mathbf{r}_2)}{|\mathbf{r}_1 - \mathbf{r}_2|} d\mathbf{r}_2 \right) |\phi_k\rangle, \quad (\text{B3})$$

such that

$$\langle \chi | \langle \phi_j | \phi_k \phi_l \rangle \equiv \langle \chi \phi_j | \phi_k \phi_l \rangle \quad (\text{B4})$$

$$= \iint \frac{\chi^*(\mathbf{r}_1) \phi_j^*(\mathbf{r}_2) \phi_k(\mathbf{r}_1) \phi_l(\mathbf{r}_2)}{|\mathbf{r}_1 - \mathbf{r}_2|} d\mathbf{r}_1 d\mathbf{r}_2. \quad (\text{B5})$$

The formulation of the full set of equations for electrons and a positron is analogous.

Now, assume that the time-dependent orbitals are expanded in a finite orthonormal basis

$$|\phi_i(t)\rangle = \sum_{\beta=1}^{N_b} C_{\beta i}(t) |\chi_\beta\rangle, \quad \langle \chi_\alpha | \chi_\beta \rangle = \delta_{\alpha\beta}, \quad (\text{B6})$$

where  $N_b$  denotes the number of basis functions. In the present case,  $\chi_\alpha(\mathbf{r})$  is a tensor product of a spherical harmonic and a

cardinal function. Projecting Eq. (B1) with  $\langle \chi_\alpha |$  we find that

$$i\dot{C}_{\alpha,i}(t) = \sum_{\gamma} h_{\alpha\gamma}(t) C_{\gamma,i}(t) + 2 \sum_{j=1}^{N_e/2} \langle \chi_\alpha \phi_j | \phi_i \phi_j \rangle - \sum_{j=1}^{N_e/2} \langle \chi_\alpha \phi_j | \phi_j \phi_i \rangle \quad (\text{B7})$$

$$= \sum_{\gamma} h_{\alpha\gamma}(t) C_{\gamma,i}(t) + 2 \sum_{\gamma} V_{\alpha\gamma}^{\text{dir}}(C(t)) C_{\gamma,i}(t) - \sum_{\gamma} V_{\alpha\gamma}^{\text{exc}}(C(t)) C_{\gamma,i}(t) \quad (\text{B8})$$

$$= \sum_{\gamma} F_{\alpha\gamma}(t, C(t)) C_{\gamma,i}(t), \quad (\text{B9})$$

where we have defined the one-body matrix elements,

$$h_{\alpha\gamma}(t) \equiv \langle \chi_\alpha | \hat{h}(t) | \chi_\gamma \rangle, \quad (\text{B10})$$

the direct and exchange matrices,

$$V_{\alpha\gamma}^{\text{dir}}(C(t)) \equiv \sum_{\beta\delta} \rho_{\beta\delta}(C(t)) u_{\gamma\delta}^{\alpha\beta} \quad (\text{B11})$$

$$V_{\alpha\gamma}^{\text{exc}}(C(t)) \equiv \sum_{\beta\delta} \rho_{\beta,\delta}(C(t)) u_{\delta\gamma}^{\alpha\beta} \quad (\text{B12})$$

$$u_{\gamma\delta}^{\alpha\beta} \equiv \langle \chi_\alpha \chi_\beta | \chi_\gamma \chi_\delta \rangle, \quad (\text{B13})$$

the time-dependent Hartree-Fock density matrix,

$$\rho_{\beta\delta}(C(t)) \equiv \sum_{j=1}^{n/2} C_{\beta j}^*(t) C_{\delta j}(t), \quad (\text{B14})$$

and the time-dependent Fock matrix,

$$F_{\alpha\gamma}(t, C(t)) \equiv h_{\alpha\gamma}(t) + 2V_{\alpha\gamma}^{\text{dir}}(C(t)) - V_{\alpha\gamma}^{\text{exc}}(C(t)). \quad (\text{B15})$$

Eq. (B9) can be written on matrix form as

$$i\dot{C}(t) = F(t, C(t))C(t), \quad (\text{B16})$$

where

$$C(t) \equiv [C_{\gamma i}(t)] \in \mathbb{C}^{N_b \times n/2}, \quad (\text{B17})$$

$$F(t, C(t)) \equiv [F_{\alpha\gamma}(t, C(t))] \in \mathbb{C}^{N_b \times N_b}. \quad (\text{B18})$$

We emphasize that Eq. (B16) is a non-linear ordinary differential equation in the sense that the matrix  $F(t, C(t))$  is dependent on the unknowns  $C(t)$ .

### 2. Implicit midpoint/Crank-Nicolson based constant density matrix schemes

In order to integrate Eq. (B16) with a given initial condition, we first observe that the presence of  $\nabla^2$  in the Fock operator leads to  $F(t, C(t))$  having eigenvalues that grow quadratically with the number of radial grid points. Explicit Runge-Kutta methods would lead to excessively stringent conditions

on the time step. A straightforward implicit method that is symplectic and in particular norm-preserving<sup>62</sup> is the implicit midpoint method, yielding

$$C^{k+1} = C^k - \frac{i\Delta t}{2} F(t_{k+\frac{1}{2}}, \bar{C}) (C^k + C^{k+1}), \quad (\text{B19})$$

where for a chosen time step  $\Delta t$ ,

$$C^k \equiv C(t_k), \quad t_k = k\Delta t, \quad k = 0, 1, \dots, k_{\text{steps}}, \quad (\text{B20})$$

$$t_{k+\frac{1}{2}} \equiv t_k + \frac{\Delta t}{2}, \quad (\text{B21})$$

$$\bar{C} \equiv \frac{1}{2} (C^k + C^{k+1}). \quad (\text{B22})$$

Re-arranging terms, Eq. (B19) can be written as

$$\left( I + \frac{i\Delta t}{2} F(t_{k+\frac{1}{2}}, \bar{C}) \right) C^{k+1} = \left( I - \frac{i\Delta t}{2} F(t_{k+\frac{1}{2}}, \bar{C}) \right) C^k, \quad (\text{B23})$$

which is a system of non-linear equations because  $F(\bar{t}, \bar{C})$  is dependent on the unknown  $C^{k+1}$  through  $\bar{C}$ . However, for a fixed  $\bar{C}$ , it is a system of *linear* equations.

To solve Eq. (B23), we approximate  $\bar{C}$ . As a first approximation, we take

$$\bar{C} = \frac{1}{2} (C^k + C^{k+1}) \approx C^k, \quad (\text{B24})$$

which can be interpreted as keeping the density matrix (B14) (and consequently the direct (B11) and exchange (B12) matrices) constant over the interval  $[t, t + \Delta t]$ , which we refer to as constant density-matrix (CDM) integration. Solving Eq. (B19) with  $\bar{C}$  given by Eq. (B24) yields an integration scheme that is accurate to first order in  $\Delta t$ , which we refer to as the CDM1 integrator.

An approximate second-order scheme, the CDM2 integrator, can be formulated using an idea of Beck and Meyer<sup>63</sup> The CDM2 integrator can be described as follows:

- (i) Solve Eq. (B19) a *half step* forwards in time (from  $[t, t + \frac{\Delta t}{2}]$ ) using Eq. (B24) for  $\bar{C}$ , i.e., solve

$$\begin{aligned} \left( I + \frac{i\Delta t}{4} F(t_{k+\frac{1}{4}}, \bar{C}) \right) \tilde{C} &= \\ \left( I - \frac{i\Delta t}{4} F(t_{k+\frac{1}{4}}, \bar{C}) \right) C^k, \end{aligned} \quad (\text{B25})$$

for  $\tilde{C}$ .

- (ii) Use the solution of Eq. (B25) as an improved estimate for  $\bar{C} \leftarrow \tilde{C}$ .

- (iii) Solve for  $C^{k+1}$  in two *half* steps:

- (a) First, solve for the midpoint  $C^{k+\frac{1}{2}}$

$$\begin{aligned} \left( I + \frac{i\Delta t}{4} F(t_{k+\frac{1}{4}}, \tilde{C}) \right) C^{k+\frac{1}{2}} &= \\ \left( I - \frac{i\Delta t}{4} F(t_{k+\frac{1}{4}}, \tilde{C}) \right) C^k \end{aligned} \quad (\text{B26})$$

- (b) Second, solve for  $C^{k+1}$

$$\begin{aligned} \left( I + \frac{i\Delta t}{4} F(t_{k+\frac{3}{4}}, \tilde{C}) \right) C^{k+1} &= \\ \left( I - \frac{i\Delta t}{4} F(t_{k+\frac{3}{4}}, \tilde{C}) \right) C^{k+\frac{1}{2}}. \end{aligned} \quad (\text{B27})$$

In practice, we have experienced that the CDM2 integrator provides significantly improved accuracy over CDM1 in the sense that results converge faster with respect to  $\Delta t$ .

The CDM1 and CDM2 integrators are applicable to the solution of the radial equations of motion for for electrons and a (single) positron given by Eqs. (23) and (24). Applying the implicit midpoint rule, the equations of motion for the electrons and the positron can be written as

$$\left( I + \frac{i\Delta t}{2} \mathcal{F}_e(t_{k+\frac{1}{2}}; \bar{u}, \bar{v}) \right) u^{k+1} = \left( I - \frac{i\Delta t}{2} \mathcal{F}_e(t_{k+\frac{1}{2}}; \bar{u}, \bar{v}) \right) u^k, \quad (\text{B28})$$

$$\left( I + \frac{i\Delta t}{2} \mathcal{F}_p(t_{k+\frac{1}{2}}; \bar{u}) \right) v^{k+1} = \left( I - \frac{i\Delta t}{2} \mathcal{F}_p(t_{k+\frac{1}{2}}; \bar{u}) \right) v^k \quad (\text{B29})$$

where  $u^n$  and  $v^n$  are the vectorization of the discretized electron and positron orbitals

$$u^k \equiv [u_0^{1,k}, \dots, u_l^{1,k}, \dots, u_l^{N_e/2,k}]^T, \quad (\text{B30})$$

$$v^k \equiv [v_0^{1,k}, \dots, v_l^{1,k}]^T \quad (\text{B31})$$

and where  $\mathcal{F}_e \in \mathbb{C}^{((N_e/2)N_r n_{lm}) \times ((N_e/2)N_r n_{lm})}$  and  $\mathcal{F}_p \in \mathbb{C}^{(N_r n_{lm}) \times (N_r n_{lm})}$  are matrices that act on the vectorization of the orbitals,  $N_r$  denotes the number of radial grid points and  $n_{lm}$  the number of angular momenta used in the expansion of the orbital.

The dimensionality of  $\mathcal{F}_e$  and  $\mathcal{F}_p$  quickly prohibits the direct solution Eqs. (B28) and (B29). Instead, we solve the linear equations iteratively with the BiConjugate Gradient Stabilized method (BiCGSTAB)<sup>64</sup> (implemented in SciPy), which requires the action of  $\mathcal{F}_e$  and  $\mathcal{F}_p$  on an orbital vector, which for the electrons is given by

$$\begin{aligned} (\mathcal{F}_e(t_{k+\frac{1}{2}}; \bar{u}, \bar{v}) u^k)^i &= \hat{h}_l^e u_l^{i,k} \\ &- iA(t_{k+\frac{1}{2}}) [a_{l-1, m_l} D_{-l} u_{l-1}^{i,k} + a_{l, m_l} D_{l+1} u_{l+1}^{i,k}] \\ &+ 2 \sum_{l'} \mathcal{D}_{l, l'}^{m_l} (r; \bar{u}) u_{l'}^{i,k} - \sum_{l'} \mathfrak{R}_{l, l'}^{m_l} (r; \bar{v}) u_{l'}^{i,k} \\ &- \sum_j \sum_{l'} \mathfrak{X}_{ij, l'}^{m_l m_j} (r; \bar{u}_j, u_i^k) \bar{u}_{l'}^{j,k} \end{aligned} \quad (\text{B32})$$

where the dependence of the exchange matrix  $\mathfrak{X}$  on both  $\bar{u}$  and  $u^k$  should be noted. For the positron

$$\begin{aligned} (\mathcal{F}_p(t_{k+\frac{1}{2}}; \bar{u}) v^k) &= \hat{h}_l^p v_l^k \\ &+ iA(t_{k+\frac{1}{2}}) [a_{l-1, 0} D_{-l} v_{l-1}^k + a_{l, 0} D_{l+1} v_{l+1}^k] \\ &- 2 \sum_{l'} \mathcal{D}_{l, l'}^0 (r; \bar{u}) v_{l'}^k. \end{aligned} \quad (\text{B33})$$

Additionally, we have found that using a preconditioner is crucial when employing the BiCGSTAB routine. The preconditioners are chosen to approximate  $\left(I + \frac{i\Delta t}{2} \mathcal{F}_e(t_{k+\frac{1}{2}}; \vec{u}, \vec{v})\right)^{-1}$  and  $\left(I + \frac{i\Delta t}{2} \mathcal{F}_p(t_{k+\frac{1}{2}}; \vec{u})\right)^{-1}$ . Exploiting that the Laplacian (and thus the kinetic energy matrix) is block-diagonal in the angular-momentum quantum number, and that the Coulomb interaction of the electrons and the positron with the nucleus is diagonal and time-independent, one can precompute the preconditioner matrices  $\mathcal{M}_e$  and  $\mathcal{M}_p$  prior to propagation. The preconditioner matrices are thus block-diagonal in  $l$ , with each  $l$ -block given by

$$\mathcal{M}_l^e = \left(I + \frac{i\Delta t}{2} H_l^e\right)^{-1}, \quad (\text{B34})$$

$$\mathcal{M}_l^p = \left(I + \frac{i\Delta t}{2} H_l^p\right)^{-1}, \quad (\text{B35})$$

where

$$H_l^e = T_l - V, \quad (\text{B36})$$

$$H_l^p = T_l + V. \quad (\text{B37})$$

Here,  $T_l$  is the matrix representation of  $-\frac{1}{2}\Delta_l$  and  $V$  is the diagonal matrix representation of the Coulomb interaction  $V = [\frac{1}{r_\alpha} \delta_{\alpha\beta}]$  in the GLL basis.

### Appendix C: Phase angles

The relative phase angles between the external electric field and the induced position expectation values of the electrons and positrons are calculated by the following steps:

1. At  $\omega = 0.01$ , we use  $t_{\text{peak}}$  to indicate the time at which the displacements of the positron and electron peaks. Due to the linear and adiabatic response at this frequency,  $t_{\text{peak}}$  also indicates the time of peak electric-field strength.
2. By making the  $\omega$ -steps sufficiently small, we can follow how  $t_{\text{peak}}$  evolves as a function of  $\omega$ .
3. We then define the phase angle as

$$\theta = \pi \frac{t_{\text{peak}} - t_{\text{max}}}{|t_{\text{min}} - t_{\text{max}}|}, \quad (\text{C1})$$

where  $t_{\text{max}} = \operatorname{argmax}_t \mathcal{E}(t)$  and  $t_{\text{min}} = \operatorname{argmin}_t \mathcal{E}(t)$ .

- <sup>1</sup>P. Moskal, B. Jasińska, E. Stępień, and S. D. Bass, "Positronium in medicine and biology," *Nat. Rev. Phys.* **1**, 527–529 (2019).
- <sup>2</sup>S. D. Bass, S. Mariazzi, P. Moskal, and E. Stępień, "Colloquium: Positronium physics and biomedical applications," *Rev. Mod. Phys.* **95**, 021002 (2023).
- <sup>3</sup>P. Moskal, A. Bilewicz, M. Das, B. Huang, A. Khreptak, S. Parzych, J. Qi, A. Rominger, R. Seifert, S. Sharma, K. Shi, W. M. Steinberger, R. Walczak, and E. Stępień, "Positronium Imaging: History, Current Status, and Future Perspectives," *IEEE Trans. Radiat. Plasma Med. Sci.* **9**, 981–1001 (2025).

- <sup>4</sup>Y. C. Jean, "Positron annihilation spectroscopy for chemical analysis: A novel probe for microstructural analysis of polymers," *Microchem. J.* **42**, 72–102 (1990).
- <sup>5</sup>G. Dlubek, J. Pionteck, V. Bondarenko, G. Pompe, C. Taesler, K. Petters, and R. Krause-Rehberg, "Positron Annihilation Lifetime Spectroscopy (PALS) for Interdiffusion Studies in Disperse Blends of Compatible Polymers: A Quantitative Analysis," *Macromolecules* **35**, 6313–6323 (2002).
- <sup>6</sup>D. W. Gidley, H.-G. Peng, and R. S. Vallery, "Positron annihilation as a method to characterize porous materials," *Annu. Rev. Mater. Res.* **36**, 49–79 (2006).
- <sup>7</sup>A. N. Singh, "Positron annihilation spectroscopy in tomorrow's material defect studies," *Appl. Spectrosc. Rev.* **51**, 359–378 (2016).
- <sup>8</sup>A. G. Attallah, V. Bon, K. Maity, R. Zaleski, E. Hirschmann, S. Kaskel, and A. Wagner, "Revisiting Metal–Organic Frameworks Porosimetry by Positron Annihilation: Metal Ion States and Positronium Parameters," *J. Phys. Chem. Lett.* **15**, 4560–4567 (2024).
- <sup>9</sup>J. Charry, M. T. d. N. Varella, and A. Reyes, "Binding Matter with Antimatter: The Covalent Positron Bond," *Angew. Chem. Int. Ed.* **57**, 8859–8864 (2018).
- <sup>10</sup>F. Moncada, L. Pedraza-González, J. Charry, M. T. d. N. Varella, and A. Reyes, "Covalent bonds in positron dihalides," *Chem. Sci.* **11**, 44–52 (2019).
- <sup>11</sup>J. Charry, F. Moncada, M. Barborini, L. Pedraza-González, M. T. d. N. Varella, A. Tkatchenko, and A. Reyes, "The three-center two-positron bond," *Chem. Sci.* **13**, 13795–13802 (2022).
- <sup>12</sup>D. Archila, F. Moncada, J. Charry, M. Varella, R. Flores-Moreno, F. J. Torres, and A. Reyes, "Two-positron-bonded dihalides: Ps<sub>2</sub>XY (X, Y=F, Cl, Br)," *Chem. Eur. J.* **30**, e202402618 (2024).
- <sup>13</sup>J. Hofierka, C. M. Cunningham, Brian Rawlins, C. H. Patterson, and D. G. Green, "Many-body theory of positron binding to polyatomic molecules," *Nature* **606**, 688–693 (2022).
- <sup>14</sup>J. A. Charry Martinez, M. Barborini, and A. Tkatchenko, "Correlated Wave Functions for Electron–Positron Interactions in Atoms and Molecules," *J. Chem. Theory Comput.* **18**, 2267–2280 (2022).
- <sup>15</sup>S. Upadhyay, A. Benali, and K. D. Jordan, "Capturing Correlation Effects in Positron Binding to Atoms and Molecules," *J. Chem. Theory Comput.* **20**, 9879–9893 (2024).
- <sup>16</sup>D. Tumakov, P. Rzhetskii, T. Shomenov, and S. Bubin, "Relativistic corrections in the ground and excited states of positronic beryllium," *Phys. Rev. A* **109**, 042826 (2024).
- <sup>17</sup>G. Gribakin, "Enhancement of positron annihilation on molecules due to vibrational Feshbach resonances," *Nuc. Inst. Meth. Phys. Res. Sec. B* **192**, 26–39 (2002).
- <sup>18</sup>G. F. Gribakin, J. A. Young, and C. M. Surko, "Positron-molecule interactions: Resonant attachment, annihilation, and bound states," *Rev. Mod. Phys.* **82**, 2557–2607 (2010).
- <sup>19</sup>J. Mitroy and G. G. Ryzhikh, "Measuring the positron affinities of atoms," *J. Phys. B* **32**, L411 (1999).
- <sup>20</sup>C. M. Surko, J. R. Danielson, G. F. Gribakin, and R. E. Continetti, "Measuring positron–atom binding energies through laser-assisted photorecombination," *New Journal of Physics* **14**, 065004 (2012).
- <sup>21</sup>P. B. Corkum and F. Krausz, "Attosecond science," *Nat. Phys.* **3**, 381–387 (2007).
- <sup>22</sup>F. Krausz and M. Ivanov, "Attosecond physics," *Rev. Mod. Phys.* **81**, 163–234 (2009).
- <sup>23</sup>M. Nisoli, P. Decleva, F. Calegari, A. Palacios, and F. Martín, "Attosecond Electron Dynamics in Molecules," *Chem. Rev.* **117**, 10760–10825 (2017).
- <sup>24</sup>Y.-X. Yan, E. B. Gamble Jr, and K. A. Nelson, "Impulsive stimulated scattering: General importance in femtosecond laser pulse interactions with matter, and spectroscopic applications," *J. Chem. Phys.* **83**, 5391–5399 (1985).
- <sup>25</sup>D. N. Fittinghoff, P. R. Bolton, B. Chang, and K. C. Kulander, "Observation of nonsequential double ionization of helium with optical tunneling," *Phys. Rev. Lett.* **69**, 2642–2645 (1992).
- <sup>26</sup>B. Walker, B. Sheehy, L. F. DiMauro, P. Agostini, K. J. Schafer, and K. C. Kulander, "Precision measurement of strong field double ionization of helium," *Phys. Rev. Lett.* **73**, 1227–1230 (1994).
- <sup>27</sup>Y. Deng, Z. Zeng, Z. Jia, P. Komm, Y. Zheng, X. Ge, R. Li, and G. Marcus, "Ultrafast excitation of an inner-shell electron by laser-induced electron recollision," *Phys. Rev. Lett.* **116**, 073901 (2016).

- <sup>28</sup>W. Becker, S. Goreslavski, D. Milošević, and G. G. Paulus, “The plateau in above-threshold ionization: the keystone of rescattering physics,” *J. Phys. B* **51**, 162002 (2018).
- <sup>29</sup>C. I. Blaga, J. Xu, A. D. DiChiara, E. Sistrunk, K. Zhang, P. Agostini, T. A. Miller, L. F. DiMauro, and C. D. Lin, “Imaging ultrafast molecular dynamics with laser-induced electron diffraction,” *Nature* **483**, 194–197 (2012).
- <sup>30</sup>A. McPherson, G. Gibson, H. Jara, U. Johann, T. S. Luk, I. A. McIntyre, K. Boyer, and C. K. Rhodes, “Studies of multiphoton production of vacuum-ultraviolet radiation in the rare gases,” *J. Opt. Soc. Am. B* **4**, 595–601 (1987).
- <sup>31</sup>M. Ferray, A. L’Huillier, X. F. Li, L. A. Lompre, G. Mainfray, and C. Manus, “Multiple-harmonic conversion of 1064 nm radiation in rare gases,” *J. Phys. B* **21**, L31 (1988).
- <sup>32</sup>M. Lewenstein, P. Balcou, M. Y. Ivanov, A. L’Huillier, and P. B. Corkum, “Theory of high-harmonic generation by low-frequency laser fields,” *Phys. Rev. A* **49**, 2117–2132 (1994).
- <sup>33</sup>I. C. D. Merritt, D. Jacquemin, and M. Vacher, “Attochemistry: Is Controlling Electrons the Future of Photochemistry?” *J. Phys. Chem. Lett.* **12**, 8404–8415 (2021).
- <sup>34</sup>T. Ditmire, J. Zweiback, V. P. Yanovsky, T. E. Cowan, G. Hays, and K. B. Wharton, “Nuclear fusion from explosions of femtosecond laser-heated deuterium clusters,” *Nature* **398**, 489–492 (1999).
- <sup>35</sup>C. Müller, K. Z. Hatsagortsyan, and C. H. Keitel, “Muon pair creation from positronium in a linearly polarized laser field,” *Phys. Rev. A* **78**, 033408 (2008).
- <sup>36</sup>Y. Suzuki, S. Hagiwara, and K. Watanabe, “Time-Dependent Multicomponent Density Functional Theory for Coupled Electron-Positron Dynamics,” *Phys. Rev. Lett.* **121**, 133001 (2018).
- <sup>37</sup>K. Lévêque-Simon, A. Camper, R. Taïeb, J. Caillat, C. Lévêque, and E. Giner, “Production of positronium chloride: A study of the charge exchange reaction between Ps and Cl<sup>-</sup>,” *J. Chem. Phys.* **160**, 104301 (2024).
- <sup>38</sup>M. W. J. Bromley and J. Mitroy, “Configuration-interaction calculations of PsH and e<sup>+</sup> Be,” *Phys. Rev. A* **65**, 012505 (2001).
- <sup>39</sup>M. W. J. Bromley and J. Mitroy, “Large-dimension configuration-interaction calculations of positron binding to the group-II atoms,” *Phys. Rev. A* **73**, 032507 (2006).
- <sup>40</sup>S. L. Saito, “Multireference configuration interaction calculations of some low-lying states of positronium hydride,” *J. Chem. Phys.* **118**, 1714–1720 (2003).
- <sup>41</sup>S. L. Saito, “Calculations for the ground states of positronium halides by singly and doubly excited configuration interaction method,” *Chem. Phys. Lett.* **381**, 565–571 (2003).
- <sup>42</sup>K. C. Kulander, “Time-dependent theory of multiphoton ionization of xenon,” *Phys. Rev. A* **38**, 778–787 (1988).
- <sup>43</sup>K. Schafer and K. Kulander, “Energy analysis of time-dependent wave functions: Application to above-threshold ionization,” *Phys. Rev. A* **42**, 5794–5797 (1990).
- <sup>44</sup>K. C. Kulander, K. J. Schafer, and J. L. Krause, “Dynamics of Short-Pulse Excitation, Ionization and Harmonic Conversion,” in *Super-Intense Laser-Atom Physics*, NATO ASI Series, edited by B. Piraux, A. L’Huillier, and K. Rzażewski (Springer, Boston, MA, 1993) pp. 95–110.
- <sup>45</sup>M. Born and R. Oppenheimer, “Zur Quantentheorie der Molekeln,” *Ann. Phys.* **389**, 457–484 (1927).
- <sup>46</sup>M. Born and K. Huang, *Dynamical Theory of Crystal Lattices* (Clarendon Press, Oxford, 1954).
- <sup>47</sup>P. E. Cade and A. Farazdel, “The electronic structure and positron annihilation characteristics of positronium halides, [X<sup>-</sup>; e<sup>+</sup>]. I. Hartree-Fock calculations and stability,” *J. Chem. Phys.* **66**, 2598–2611 (1977).
- <sup>48</sup>H. A. Kurtz and K. D. Jordan, “Theoretical studies of positron complexes with atomic anions,” *J. Chem. Phys.* **72**, 493–503 (1980).
- <sup>49</sup>B. H. Bransden and C. J. Joachain, *Physics of atoms and molecules*, 2nd ed. (Prentice Hall, Harlow, England, 2003).
- <sup>50</sup>T. Sato, K. L. Ishikawa, I. Březinová, F. Lackner, S. Nagele, and J. Burgdörfer, “Time-dependent complete-active-space self-consistent-field method for atoms: Application to high-order harmonic generation,” *Physical Review A* **94**, 023405 (2016).
- <sup>51</sup>M. Cinal, “Highly accurate numerical solution of Hartree-Fock equation with pseudospectral method for closed-shell atoms,” *J. Math. Chem.* **58**, 1571–1600 (2020).
- <sup>52</sup>D. Hochstuhl, C. M. Hinz, and M. Bonitz, “Time-dependent multiconfiguration methods for the numerical simulation of photoionization processes of many-electron atoms,” *Eur. Phys. J. Spec. Top.* **223**, 177–336 (2014).
- <sup>53</sup>I. Barth and C. Lasser, “Trigonometric pulse envelopes for laser-induced quantum dynamics,” *J. Phys. B* **42**, 235101 (2009).
- <sup>54</sup>S. L. Saito, “Is positronium hydride atom or molecule?” *Nucl. Instrum. Methods Phys. Res. B* **171**, 60–66 (2000).
- <sup>55</sup>P. Ehrenfest, “Bemerkung über die angenäherte Gültigkeit der klassischen Mechanik innerhalb der Quantenmechanik,” *Z. Phys.* **45**, 455–457 (1927).
- <sup>56</sup>G. G. Paulus, W. Becker, W. Nicklich, and H. Walther, “Rescattering effects in above-threshold ionization: a classical model,” *J. Phys. B* **27**, L703 (1994).
- <sup>57</sup>J. P. Boyd, *Chebyshev and Fourier spectral methods* (Dover, New York, 2001).
- <sup>58</sup>T. N. Rescigno and C. W. McCurdy, “Numerical grid methods for quantum-mechanical scattering problems,” *Phys. Rev. A* **62**, 032706 (2000).
- <sup>59</sup>A. D. Bandrauk and M. Ivanov, *Quantum Dynamic Imaging: Theoretical and Numerical Methods* (Springer, New York, 2011).
- <sup>60</sup>“Numpy polynomial legendre,” (2025), accessed on December 19, 2025.
- <sup>61</sup>The sign for the differentiation matrix at the boundary points  $\tilde{C}_0^f(\xi_0)$  and  $\tilde{C}_N^f(\xi_N)$  given in Refs. 51,57 is wrong. They should be opposite.
- <sup>62</sup>E. Hairer, C. Lubich, and G. Wanner, *Geometric Numerical Integration* (Springer, Berlin, 2006).
- <sup>63</sup>M. H. Beck and H.-D. Meyer, “An efficient and robust integration scheme for the equations of motion of the multiconfiguration time-dependent Hartree (MCTDH) method,” *Z. Phys. D* **42**, 113–129 (1997).
- <sup>64</sup>R. Barrett, M. Berry, T. F. Chan, J. Demmel, J. Donato, J. Dongarra, V. Eijkhout, R. Pozo, C. Romine, and H. Van der Vorst, *Templates for the Solution of Linear Systems: Building Blocks for Iterative Methods* (SIAM, Philadelphia, 1994).